

EFFECTS OF INTEGRATIONS AND ADAPTIVITY FOR THE EULERIAN–LAGRANGIAN METHOD*

Jiwei Jia

LMAM & School of Mathematical Science, Peking University, Beijing 100871, China

Email: jiajiwei@math.pku.edu.cn

Xiaozhe Hu

Beijing International Center for Mathematical Research, Beijing 100871, China

Email: huxiaozhezju@gmail.com

Jinchao Xu

Department of Mathematics, Pennsylvania State University, University Park, PA, 16802, USA

Email: xu@math.psu.edu

Chen-Song Zhang

School of Mathematical Sciences, Peking University, Beijing 100871, China

Email: zhangchensong@gmail.com

Abstract

This paper provides an analysis on the effects of exact and inexact integrations on stability, convergence, numerical diffusion, and numerical oscillations for the Eulerian–Lagrangian method (ELM). In the finite element ELM, when more accurate integrations are used for the right-hand-side, less numerical diffusion is introduced and better approximation is obtained. When linear interpolation is used for numerical integrations, the resulting ELM is shown to be unconditionally stable and of first-order accuracy. When Gauss quadrature is used, conditional stability and second-order accuracy are established under some mild constraints for the convection-diffusion problems. Finally, numerical experiments demonstrate that more accurate integrations lead to better approximation, and spatial adaptivity can substantially reduce numerical oscillations and smearing that often occur in the ELM when inexact numerical integrations are used.

Mathematics subject classification: 65M25, 65M60.

Key words: Convection-diffusion problems; Eulerian–Lagrangian method; Adaptive mesh refinement.

1. Introduction

In many physical problems, convection dominates diffusion; for these nearly hyperbolic problems, classical Galerkin finite element methods may suffer from instability and it is natural to explore the method of characteristics (MoC). It is well-known, however, that deformation of mesh in the pure Lagrangian framework could lead to deterioration of accuracy of the numerical solution. The finite element Eulerian–Lagrangian method (ELM) [1, 2] seeks the position of a particle at previous time that reaches a certain point at current time. Thus, the diffusion operator is always solved on a fixed mesh, eliminating the need for mesh regeneration. This method has many variants (see [3, 4] and references therein); and, it is also known as the semi-Lagrangian method (SLM) in the meteorological community (cf. [5]).

* Received April 26, 2010 / Revised version received October 11, 2010 / Accepted December 8, 2010 /
Published online June 27, 2011 /

The ELM has several desirable features: (a) it allows relatively large time-step size; (b) it results in a symmetric positive definite discrete linear system, which allows usage of available optimal iterative solvers; (c) it treats (linear or nonlinear) convection terms in a uniform way and the nonlinearity can be handled by solving various ordinary differential equations (ODEs), which can be done in parallel easily.

Despite of all these advantages, the ELM is known to have several disadvantages: (1) it is sensitive to the accuracy of integration/interpolation; (2) it can introduce certain level of numerical diffusion in practice; (3) its computational overhead for back tracking is usually heavy. We refer to [6–8] and the reference therein for more details. Indeed, (1) and (2) are essentially related. Usually, the finite difference ELMs are more diffusive when first-order interpolation schemes are employed; this is similar to the upwinding scheme [9]. In the finite element framework, numerical diffusion is much smaller. We can expect that numerical diffusion can be reduced when more accurate integrations are used on the right-hand-side of finite element weak formulation. In particular, for a simple one-dimensional case, we prove that the ELM is free of numerical diffusion when the right-hand-side is integrated exactly; see Section 3. For more general cases, our numerical experiments also confirms this expectation; see Section 6.

There have been discussions on the convergence and stability of the ELM; we refer to [1, 2, 10, 11] for a priori error estimations, and [12, 13] for studies on numerical stability. Most analysis on this method in the literature have been carried out under the assumption that all integrations are evaluated exactly. However, numerical quadratures often have to be used to evaluate these integrations for two- and three-dimensional problems in practice. Without the exact-integration assumption, analysis of the ELM is much more involved. To the best of our knowledge, [12] and [13] are the only papers that analyzed the effect of numerical quadratures theoretically. More specifically, [12] studied how the stability of the ELM is compromised by some classical quadrature rules in one dimensional case for pure transport problems.

A posteriori error analysis and spatial mesh adaptivity have been applied to the ELM; see [14–17]. In particular, [16] gave a residual-based $L^2(L^2)$ a posteriori error estimator; however, the numerical experiments therein indicated that the norm of the residual on an individual element may be a poor estimate of the local error (the norm of the residual can be used to bound the error on a global basis from above.) In [17], the authors derived a sharp $L^\infty(L^1)$ a posteriori error estimator for a nonlinear convection-diffusion equation, which is discretized with the ELM implicitly in time and the continuous piecewise linear finite element in space. We will use the spatial error estimators proposed in [17] to drive out adaptive mesh refinements in Sections 5 and 6.

In this paper, we make the following observations on ELM with inexact numerical integrations through theoretical analysis and numerical experiments:

- *Numerical diffusion and dispersion.* We observe that, when exact integration is employed, very little numerical diffusion and dispersion are introduced by ELM. On the other hand, ELM with linear interpolations tends to introduce excessive numerical diffusion.
- *Stability and convergence rate.* We show the conditional stability and optimal convergence rate for ELM with Gauss quadratures, and unconditional stability and suboptimal convergence rate for ELM with linear interpolations.
- *Effects of adaptive mesh refinement.* The adaptive mesh refinement can not only stabilize the scheme but also reduce numerical diffusion.

The rest of the present paper is organized as follows. In Section 2, we introduce a model convection-diffusion problem and its Eulerian–Lagrangian discretization. In Section 3, we give an analysis of numerical diffusion and numerical dispersion introduced by the ELM with exact integrations. In Section 4, we discuss numerical stability, numerical diffusion, numerical dispersion, and convergence of the ELM with inexact integrations. In Sections 5 and 6, we discuss the effects of adaptivity on the ELM, with numerical experiments, in one and two space dimensions, respectively. Finally, we summarize with a few concluding remarks in Section 7.

2. The Eulerian–Lagrangian Method

Consider a bounded domain $\Omega \subset \mathbb{R}^d$ ($d = 1, 2, 3$) with Lipschitz boundary $\partial\Omega$. We denote the Banach space of real-valued Lebesgue-measurable functions by $L^p(\Omega)$, and its norm by $\|\cdot\|_{L^p(\Omega)}$, $1 \leq p \leq \infty$; for $p = 2$, we drop the subscript and denote the L^2 -norm by $\|\cdot\|$. We denote, by $W^{k,p}(\Omega)$, the Sobolev spaces with norm

$$\|u\|_{W^{k,p}(\Omega)} := \left(\sum_{|\alpha| \leq k} \|D^\alpha u\|_{L^p(\Omega)}^p \right)^{\frac{1}{p}} \quad (1 \leq p < \infty) \quad \text{and} \quad \|u\|_{W^{k,\infty}(\Omega)} := \operatorname{esssup}_{|\alpha| \leq k} \{ \|D^\alpha u\|_{L^\infty(\Omega)} \},$$

where $\alpha = (\alpha_1, \dots, \alpha_d)$ is a multi-index, $|\alpha| := \sum_{j=1}^d \alpha_j$, and $D^\alpha := \partial_{x_1}^{\alpha_1} \dots \partial_{x_d}^{\alpha_d}$ is the weak derivative. When $p = 2$, we denote $W^{k,p}(\Omega)$ by $H^k(\Omega)$ and $H_0^k(\Omega) := \{u \in H^k(\Omega) : u|_{\partial\Omega} = 0\}$. Furthermore, we write the H^k -norm and its corresponding semi-norm as $\|\cdot\|_k$ and $|\cdot|_k$, respectively. For a given Banach space V with norm $\|\cdot\|_V$, we denote, by $L^p(0, T; V)$, the space of L^p integrable functions from $[0, T]$ into V with norm

$$\|u\|_{L^p(0,T;V)} := \left(\int_0^T \|u\|_V^p dt \right)^{\frac{1}{p}} \quad (1 \leq p < \infty) \quad \text{and} \quad \|u\|_{L^\infty(0,T;V)} := \operatorname{esssup}_{0 \leq t \leq T} \|u(\cdot, t)\|_V.$$

Following Xu [18], we use the following notation: for two positive quantities A and B , the symbol $A \lesssim B$ means that, there is a constant C , which is independent of ε and the discretization parameter h and Δt , such that $A \leq C \cdot B$ holds. $A \approx B$ means both $A \lesssim B$ and $B \lesssim A$ hold.

2.1. A model problem

Consider the following convection-diffusion problem:

$$u_t + b \cdot \nabla u - \varepsilon \Delta u = 0, \quad x \in \Omega, \quad t \in (0, T], \quad (2.1a)$$

$$u(x, t) = g(x), \quad x \in \partial\Omega, \quad t \in [0, T], \quad (2.1b)$$

$$u(x, 0) = u_0(x), \quad x \in \Omega, \quad (2.1c)$$

where $b(x, t)$ is a given velocity field and $\varepsilon \geq 0$ is the diffusion coefficient. Furthermore, we assume that b is divergence-free, and $\|b\|_{L^\infty} + \|\nabla b\|_{L^\infty} \leq C_b$, where C_b is a constant.

We define the particle trajectory $y(x, s; t)$ for $x \in \Omega$, $s \in (0, T]$, as the solution of the following initial value problem:

$$\frac{d}{dt} y(x, s; t) = b(y(x, s; t), t), \quad y(x, s; s) = x. \quad (2.2)$$

By introducing the material derivative

$$\frac{Du}{Dt} := u_t + b \cdot \nabla u, \quad (2.3)$$

we can rewrite Eq. (2.1a) in the characteristic form

$$\frac{Du}{Dt} - \varepsilon \Delta u = 0. \tag{2.4}$$

2.2. The Eulerian–Lagrangian discretizations

Consider a uniform time grid $t^n = n\Delta t$, $n = 0, 1, 2, \dots$. We apply the backward Euler scheme for the material derivative defined in (2.3). Then we can rewrite (2.4) in the weak form for the temporal semi-discretization scheme as:

$$\left(\frac{u^{n+1} - u_*^n}{\Delta t}, v \right) + \varepsilon (\nabla u^{n+1}, \nabla v) = 0, \quad \forall v \in H_0^1(\Omega),$$

where u^{n+1} is an approximation of $u(x, t^{n+1})$ at time level t^{n+1} and $u_*^n = u^n(y(x, t^{n+1}; t^n))$.

Let \mathcal{T}_h be a quasi-uniform partition of Ω with mesh size h and V_h be the continuous piecewise linear finite element space on \mathcal{T}_h . In 1D, we denote the computational domain as $[L, R]$ and define the spatial grids as $\{x_j\}_{j=0}^N$. The full-discretization scheme for (2.1) reads: find $u_h^{n+1} \in V_h$, such that

$$(u_h^{n+1}, v_h) + \varepsilon \Delta t (\nabla u_h^{n+1}, \nabla v_h) = (u_{h,*}^n, v_h), \quad \forall v_h \in V_h \tag{2.5}$$

where $u_{h,*}^n = u_h^n(y(x, t^{n+1}; t^n))$. To simplify the discussion, we eliminate the effects of the accuracy of finding characteristic-feet and assume that we solve (2.2) exactly throughtout this paper.

We assemble the coefficient matrix on the left-hand side of (2.5) using exact integrations; and denote the coefficient matrix by K . In the rest of this paper, we use the notation: $\nu = b\Delta t/h$ and $\rho = \varepsilon\Delta t/h^2$; ν is also known as the CFL number and ρ as the Peclét number.

2.3. A priori error estimates

We refer to the work in [1, Theorem 2] for the a priori error estimation for (2.5) (for $\varepsilon > 0$) under the assumption that all the integrations in the weak form (2.5) are evaluated exactly: If the solution u satisfies (a) $u \in L^\infty(0, T; W^{q,2}(\mathbb{R}))$, (b) $\frac{\partial u}{\partial t} \in L^2(0, T; W^{q-1+\theta,2}(\mathbb{R}))$, $\theta = 1$, if $q = 2$ and $\theta = 0$, if $q > 2$, (c) $\frac{\partial^2 u}{\partial t^2} \in L^2(0, T; L^2(\mathbb{R}))$, then the continuous piecewise linear finite element solution u_h satisfies that

$$\begin{aligned} \max_{0 \leq t^n \leq T} \|(u - u_h)(t^n)\| &\leq C_1 \left\| \frac{D^2 u}{Dt^2} \right\|_{L^2(\mathbb{R} \times [0, T])} \Delta t \\ &+ \frac{C_2}{\sqrt{\varepsilon}} \left(\left\| \frac{\partial u}{\partial t} \right\|_{L^2(0, T; W^{q-1+\theta,2}(\mathbb{R}))} + \|u\|_{L^\infty(0, T; W^{q,2}(\mathbb{R}))} \right) h^q. \end{aligned}$$

[2] gave an ε -uniform a priori error estimation for the Navier-Stokes equation and proved the error in a discrete energy norm $\|\cdot\| := (\|\cdot\|^2 + \varepsilon\Delta t|\cdot|_1^2)^{\frac{1}{2}}$ is

$$\begin{aligned} \max_{0 \leq t^n \leq T} \|(u - u_h)(t^n)\| &\leq C_3 \left\| \frac{D^2 u}{Dt^2} \right\|_{L^2(\mathbb{R} \times [0, T])} \Delta t \\ &+ e^{\|\nabla u\|_{L^\infty(0, T; L^\infty(\mathbb{R}))}} \left[C_4 \|u\|_{L^\infty(0, T; W^{2,\infty}(\mathbb{R}))} \frac{h^2}{\Delta t} \right. \\ &\left. + C_5 \|\nabla(\nabla u)\|_{L^\infty(0, T; L^\infty(\mathbb{R}))} \|\nabla u\|_{L^\infty(0, T; L^\infty(\mathbb{R}))}^2 \left(\varepsilon h + \frac{h^2}{\Delta t} \right) \right]. \end{aligned}$$

Here $C_i, i = 1, 2, \dots, 5$ are constants and independent of $h, \Delta t$ and ε .

When numerical methods do not yield integrations exactly, the convergence result is more difficult to obtain; see Section 4 for the details.

2.4. One-dimensional benchmark problems

We introduce two benchmark problems, which will be used for the testing purpose in this paper.

Problem 2.1. *Given the initial condition*

$$u(x, 0) = \begin{cases} 1, & x \leq 0, \\ 0, & x > 0, \end{cases}$$

the exact solution for the model problem (2.1) (if b is constant) is given by

$$u(x, t) = \frac{1}{2} \left\{ \operatorname{erfc} \left(\frac{x - bt}{2\sqrt{\varepsilon t}} \right) + \exp \left(\frac{bx}{\varepsilon} \right) \operatorname{erfc} \left(\frac{x + bt}{2\sqrt{\varepsilon t}} \right) \right\},$$

where $\operatorname{erfc}(x) = \frac{2}{\sqrt{\pi}} \int_x^\infty e^{-s^2} ds$ is the so-called complementary error function. The computational domain is $[0, 2]$, and we give the Dirichlet boundary condition $u(0) = 1, u(2) = 0$.

Problem 2.2. *Given the initial condition*

$$u(x, 0) = e^{-(x-x_0)^2/2\lambda^2},$$

the exact solution for the model problem (2.1) (if b is constant) is given by

$$u(x, t) = \frac{\lambda}{\sqrt{\lambda^2 + 2\varepsilon t}} e^{-(x-x_0-bt)^2/2(\lambda^2+2\varepsilon t)},$$

where λ is a parameter measures the width of the support of the solution. The computational domain is $[-1, 2]$, and we give the Dirichlet boundary condition $u(-1) = u(2) = 0$.

3. The ELM with Exact Integrations

In this section, we consider the one-dimensional model problem (2.1) with a constant velocity b . In this case, it is easy to evaluate all the integrations in (2.5) exactly.

3.1. Stability

The unconditional L^2 -stability of the ELM has been proven in [2] under the assumption that all the integrations are evaluated exactly. The proof is straightforward: By taking $v_h = u_h^{n+1}$ in (2.5) and applying the Cauchy–Schwarz inequality, we obtain that

$$\|u_h^{n+1}\| \leq \|u_{h,*}^n\|;$$

and, “=” holds if and only if the solution is a constant or $\varepsilon = 0$. Since b is divergence-free, the determinant of the Jacobian of the transformation $x \rightarrow y(x, t; s)$ is equal to 1 (see, for example, [19]), we have

$$\|u_h^{n+1}\| \leq \|u_{h,*}^n\| = \|u_h^n\|,$$

which means the ELM with exact integration is unconditionally stable.

3.2. Numerical diffusion and oscillations

Now we consider the artificial diffusion and dispersion terms introduced in scheme (2.5) by analyzing its modified equation, which represents the actual partial differential equation solved by scheme (2.5) (see [20]). We find that there is neither additional second- nor third-order terms in the modified equation. This observation suggests that the ELM with exact integrations only introduces small numerical diffusion and oscillations. For simplicity, we assume that the Courant number $\nu = \frac{b\Delta t}{h} \leq 1$ in this section.

Let $\phi_j(x)$ be the nodal basis function at grid point x_j . We divide the inner product $(u_{h,*}^n, \phi_j)$ into four parts and integrate each of them. Then, the right-hand-side (RHS) of (2.5) reads

$$\text{RHS} = R_1 h(u_{j-1}^n - u_{j-2}^n) + R_2 h(u_j^n - u_{j-1}^n) + R_3 h(u_{j+1}^n - u_j^n) + h u_j^n,$$

where we define $u_j^n = u_h^n(x_j)$, and

$$R_1 = -\frac{1}{6}\nu^3, \quad R_2 = \frac{1}{2}\nu^3 - \frac{1}{6}(1 + \nu)^3, \quad R_3 = \frac{1}{6}(1 - \nu)^3.$$

For the left-hand-side (LHS) of (2.5), we define $\delta^2 u_j^n := u_{j+1}^n - 2u_j^n + u_{j-1}^n$ and get

$$\text{LHS} = h \left[1 + \left(\frac{1}{6} - \rho \right) \delta^2 \right] u_j^{n+1}, \tag{3.1}$$

where $\rho = \varepsilon \Delta t / h^2$ for short. Then we can write scheme (2.5) in the following form

$$\left[1 + \left(\frac{1}{6} - \rho \right) \delta^2 \right] u_j^{n+1} = R_3 u_{j+1}^n + (R_2 - R_3 + 1) u_j^n + (R_1 - R_2) u_{j-1}^n - R_1 u_{j-2}^n.$$

We apply the general procedure in [20] to obtain the modified equation of (2.5), we then arrive at the following result:

Theorem 3.1. *The modified equation of scheme (2.5) is*

$$u_t + b u_x - \varepsilon u_{xx} + M_1 u_{xxxx} + M_2 u_{xxxxx} + \mathcal{O}(h^5) = 0, \tag{3.2}$$

where

$$M_1 = \frac{bh^3}{24} \nu(1 - \nu)^2 + \frac{1}{12} \varepsilon h^2 - \frac{1}{2} \varepsilon^2 \Delta t, \quad M_2 = \frac{bh^4}{180} (3\nu^2 - 3\nu - 1)(2\nu - 1)(\nu - 1). \tag{3.3}$$

An interesting observation from (3.3) is that, for pure convection problem (i.e. $\varepsilon = 0$), when we take $\nu = 1$, there is neither fourth- nor fifth-order terms in the modified equation (3.2). Hence, we can get a numerical approximation without numerical diffusion and oscillations. In order to check the effect of numerical diffusion, we can consider:

$$(u_t + b u_x, u) = 0 \quad \implies \quad \frac{d}{dt} \int_{\mathbb{R}} \frac{1}{2} |u|^2 = 0.$$

Hence, the L^2 -norm of the exact solution is conservative. If there is numerical diffusion introduced by the numerical scheme, then the L^2 -norm of the numerical solution should decay in time (here we use the fact that the velocity field is divergence-free, and the solution of Problem 2.2 has compact support, see [19] for details). So we can use the behavior of L^2 -norm of u_h to measure the effect of numerical diffusion. Using Problem 2.2 as a test example, we find that

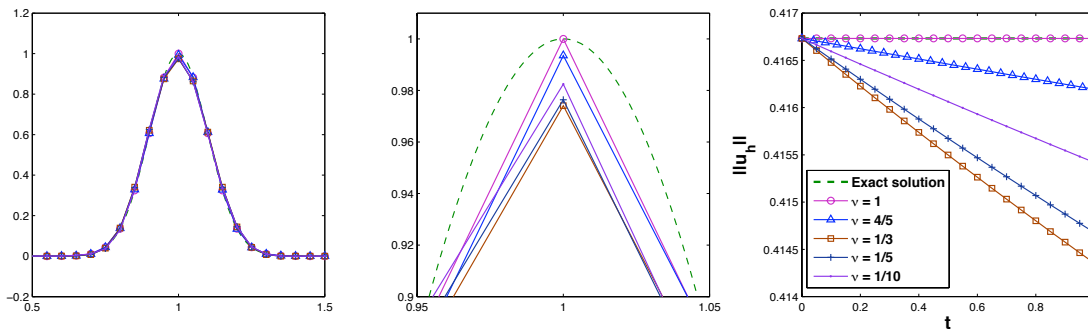


Fig. 3.1. Using exact integration to solve Problem 2.2 ($\varepsilon = 0$, $b = 1$, $h = 5 \times 10^{-2}$, $\lambda = 1/10$ and $T = 1.0$.) Left: the exact and numerical solutions; Middle: zoom in; Right: L^2 -norm of the solutions.

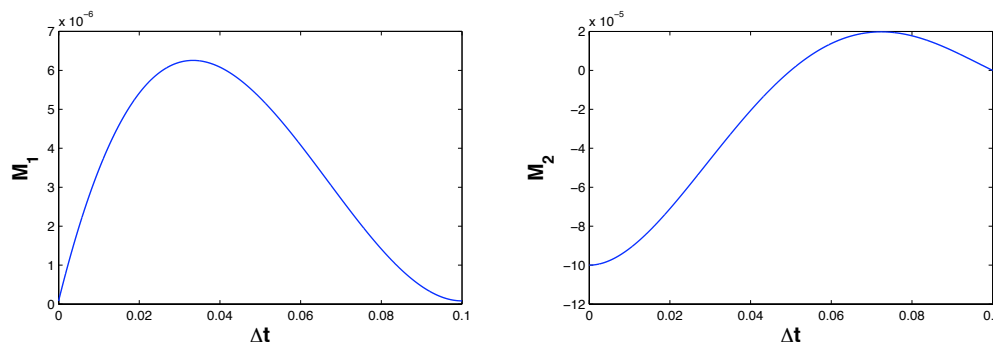


Fig. 3.2. The behavior of M_1 and M_2 with respect to Δt for fixed $h = 0.1$, $\varepsilon = 10^{-4}$.

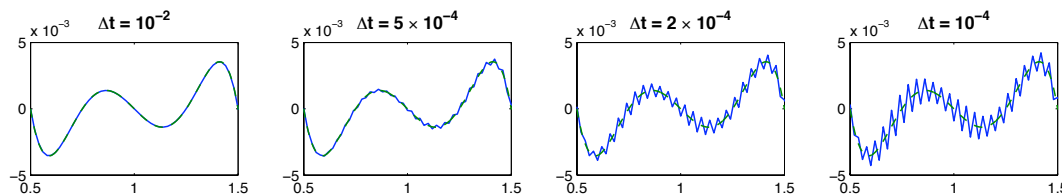


Fig. 3.3. Using exact integrations to solve a fifth-order polynomial $P_5(x, t)$. Solid line: numerical solution; dashed line: exact solution. ($\varepsilon = 0$, $b = 1$, $h = 2 \times 10^{-2}$ and $T = 0.5$, the computational domain is $[0, 2]$, we zoom in to the interested region.)

the L^2 -norm of the solution remains a constant for $\nu = 1$ (i.e., $M_1 = 0$.) According to (3.3), M_1 has a local maximum at $\nu = 1/3$ and we can see, from Fig 3.1, that $\|u_h\|$ decreases fastest for $\nu = 1/3$.

Another observation from (3.3) is that, for the convection-dominated or pure convection cases (ε is very small, then the term $-\frac{1}{2}\varepsilon^2\Delta t$ is also very small, we ignore its effect), as Δt goes to zero, the coefficient M_1 decreases to $\frac{1}{12}\varepsilon h^2$; but the magnitude of the fifth-order term M_2 increases to $\frac{bh^4}{180}$ (see Fig. 3.2). Hence, relatively big h gives numerical oscillations. This expectation is confirmed by a simple numerical test: Assume the exact solution is a fifth-order polynomial in space, $P_5(x, t) = (x - t - 1)(x - t - \frac{3}{4})(x - t - \frac{1}{2})(x - t - \frac{1}{4})(x - t)$. For this solution, we can get rid of the influence of the terms of order higher than 5 in the modified equation (3.2). The numerical solutions obtained with different time-step sizes on a fixed uniform mesh are plotted in Fig. 3.3. In this figure, we find that, if $\Delta t = 10^{-2}$ (i.e., $\nu = 1/2$),

there is no oscillation at all; oscillations appear and get larger as Δt decreases. This coincides with the theoretical expectation.

We now summarize this section with a few simple observations.

Remark 3.1. Compared with the original equation (2.1a), the modified equation (3.2) has *no* additional second- and third-order derivative terms. To measure the numerical diffusive and dispersive effects, we look at the higher-order derivative terms, u_{xxxx} and u_{xxxxx} with coefficients M_1 and M_2 . The magnitudes of M_1 and M_2 are very small ($\mathcal{O}(h^3)$ and $\mathcal{O}(h^4)$ when $\varepsilon = 0$, respectively.) However, in some extreme cases (when $\Delta t \ll h$, see Fig3.3), there may appear numerical oscillations.

Remark 3.2. We can see that M_1 is a quadratic function w.r.t. ε . If $b = 1, \nu = 1$, then M_1 is non-negative when $h \geq 6\varepsilon$; this positive diffusion coefficient is a helping term for stability. On the other hand, when h is small compared with ε , M_1 could be negative. In this case, the effect of the diffusion term in (2.1a) dominates, and the effect of the negative diffusion is neglectable.

Remark 3.3. It is easy to see that the diagonal and off-diagonal entries of the j -th row of the coefficient matrix K of the discretized linear system of (2.5) are

$$K_{jj} = \frac{2\varepsilon\Delta t}{h} + \frac{2h}{3} \quad \text{and} \quad K_{jk} = -\frac{\varepsilon\Delta t}{h} + \frac{1}{6}h \quad (k = j - 1 \text{ or } j + 1).$$

If $h < \sqrt{6\varepsilon\Delta t}$, K is an M-matrix, which guarantees the discrete maximum principle and leads to oscillation-free numerical solutions; see [21] for the details.

4. The ELM with Inexact Integrations

In this section, we discuss the effects of inexact integrations on stability, convergence, numerical diffusion, and oscillations. For the piecewise continuous linear finite element discretization, the RHS of (2.5) is an integration of two piecewise functions on two different meshes; we can evaluate it exactly for some very special cases. In general, we employ numerical approximation for it. Here we discuss two simple and easy-to-implement approaches, namely, the nodal interpolation approach and the Gauss quadrature approach.

4.1. Approach I: nodal interpolation approach

Let u_h^n be the numerical solution at the time level n for Approach I. Let $I_h : C(\Omega) \rightarrow V_h$ be the nodal interpolation of $u_{h,*}^n$, i.e.,

$$I_h u_{h,*}^n(x) = \sum_j u_h^n(y_j) \phi_j(x), \quad (4.1)$$

where $y_j = y(x_j, t^{n+1}; t^n)$. Then u_h^{n+1} satisfies that

$$(u_h^{n+1}, v) + \varepsilon\Delta t(\nabla u_h^{n+1}, \nabla v) = (I_h u_{h,*}^n, v). \quad (4.2)$$

Note that $I_h u_{h,*}^n$ and u_h^n are both piecewise linear functions on \mathcal{T}_h . Now we can compute $(I_h u_{h,*}^n, v)$ exactly. For simplicity, we denote $u_j^n = u_h^n(x_j)$ in Section 4.1.1, 4.1.2 and 4.1.3.

4.1.1. Stability: on uniform meshes

In this section, we prove the stability of scheme (4.2). For the 1D case, assuming that the velocity field b is a constant, we have the following theorem.

Theorem 4.1. *Scheme (4.2) is unconditionally stable in the von Neumann sense for the one-dimensional constant-coefficient case.*

Proof. We denote the integer and fractional part of ν by ν_I and ν_F , then (4.2) can be rewritten as

$$\left[1 + \left(\frac{1}{6} - \rho\right) \delta^2\right] u_j^{n+1} = (1 - \nu_F) \left(1 + \frac{1}{6} \delta^2\right) u_{j-\nu_I}^n + \nu_F \left(1 + \frac{1}{6} \delta^2\right) u_{j-\nu_I-1}^n. \tag{4.3}$$

Apply the discrete Fourier analysis on (4.3), we have

$$\left(1 - \frac{2}{3} s^2 + 4\rho s^2\right) G = (1 - \nu_F) \left(1 - \frac{2}{3} s^2\right) e^{-i\nu_I h \xi} + \nu_F \left(1 - \frac{2}{3} s^2\right) e^{-i(\nu_I+1)h \xi}, \tag{4.4}$$

where $i = \sqrt{-1}$, $s = \sin(\xi h/2)$, ξ is the wave number, and G is the amplification factor. Note that $s^2 \leq 1$, $\rho > 0$, and $|e^{-i\nu_I h \xi}| = |e^{-i(\nu_I+1)h \xi}| = 1$. Take the absolute value on (4.4), we get

$$\left|1 - \frac{2}{3} s^2 + 4\rho s^2\right| |G| \leq |\nu_F (1 - \frac{2}{3} s^2) e^{-i\nu_I h \xi}| + |(1 - \nu_F) (1 - \frac{2}{3} s^2) e^{-i(\nu_I+1)h \xi}| = \left|1 - \frac{2}{3} s^2\right|.$$

Then we obtain

$$|G| \leq \frac{\left|1 - \frac{2}{3} s^2\right|}{\left|1 - \frac{2}{3} s^2 + 4\rho s^2\right|} \leq 1,$$

which completes the proof. □

As a consequence, we can show the L^2 stability:

Corollary 4.1. *The scheme (4.2) is L^2 stable on \mathbb{R} .*

Remark 4.1. A direct way to show L^2 -stability of Approach I on \mathbb{R} can be derived: Consider the one-dimensional constant-coefficient case on \mathbb{R} ,

$$I_h u_{h,*}^n = \sum_j \left[(1 - \nu_F) u_{j-\nu_I}^n + \nu_F u_{j-\nu_I-1}^n \right] \phi_j,$$

thus

$$\|I_h u_{h,*}^n\| \leq (1 - \nu_F) \left\| \sum_j u_{j-\nu_I}^n \phi_j \right\| + \nu_F \left\| \sum_j u_{j-\nu_I-1}^n \phi_j \right\|.$$

Note that when we take $\|\cdot\|$ on \mathbb{R} , we have

$$\left\| \sum_j u_{j-\nu_I}^n \phi_j \right\| = \|u_h^n\| \quad \text{and} \quad \left\| \sum_j u_{j-\nu_I-1}^n \phi_j \right\| = \|u_h^n\|.$$

Hence, we get that $\|I_h u_{h,*}^n\| \leq \|u_h^n\|$. In (4.2), let $v = u_h^{n+1}$, drop the term $\varepsilon \Delta t \|\nabla u_h^{n+1}\|^2$ and apply the Cauchy–Schwarz inequality, we obtain that

$$\|u_h^{n+1}\| \leq \|I_h u_{h,*}^n\| \leq \|u_h^n\|,$$

which gives the L^2 -stability.

Now we extend the stability result in Theorem 4.1 to a uniform square grid in \mathbb{R}^2 , i.e. $h_x = h_y = h$, and assume that the velocity field $b = (b_x, b_y)^T$ is a constant vector.

Theorem 4.2. *Scheme (4.2) with bilinear element is unconditionally stable in the von Neumann sense for the two-dimensional constant-coefficient case on a uniform square grid.*

Proof. For $\nu_x = \frac{b_x \Delta t}{h} \leq 1, \nu_y = \frac{b_y \Delta t}{h} \leq 1$, we can rewrite scheme (4.2) as,

$$\begin{aligned} & (M + \varepsilon \Delta t A) u_{k,l}^{n+1} \\ &= M \left[(1 - \nu_x)(1 - \nu_y) u_{k,l}^n + (1 - \nu_x) \nu_y u_{k,l-1}^n + \nu_x (1 - \nu_y) u_{k-1,l}^n + \nu_x \nu_y u_{k-1,l-1}^n \right] \end{aligned} \quad (4.5)$$

where $u_{k,l}^n = u_h^n(x_k, y_l)$. Here

$$A u_{k,l} = \begin{bmatrix} -\frac{1}{3} & -\frac{1}{3} & -\frac{1}{3} \\ -\frac{1}{3} & \frac{8}{3} & -\frac{1}{3} \\ -\frac{1}{3} & -\frac{1}{3} & -\frac{1}{3} \end{bmatrix} : \begin{bmatrix} u_{k-1,l+1} & u_{k,l+1} & u_{k+1,l+1} \\ u_{k-1,l} & u_{k,l} & u_{k+1,l} \\ u_{k-1,l-1} & u_{k,l-1} & u_{k+1,l-1} \end{bmatrix},$$

and

$$M u_{k,l} = h^2 \begin{bmatrix} \frac{1}{36} & \frac{1}{9} & \frac{1}{36} \\ \frac{1}{9} & \frac{4}{9} & \frac{1}{9} \\ \frac{1}{36} & \frac{1}{9} & \frac{1}{36} \end{bmatrix} : \begin{bmatrix} u_{k-1,l+1} & u_{k,l+1} & u_{k+1,l+1} \\ u_{k-1,l} & u_{k,l} & u_{k+1,l} \\ u_{k-1,l-1} & u_{k,l-1} & u_{k+1,l-1} \end{bmatrix},$$

where “:” denotes the tensor product.

Apply the discrete Fourier transformation on (4.5), we obtain

$$\begin{aligned} & (C_M + \varepsilon \Delta t C_A) G \\ &= C_M \left[(1 - \nu_x)(1 - \nu_y) + (1 - \nu_x) \nu_y e^{-i\eta h} + \nu_x (1 - \nu_y) e^{-i\xi h} + \nu_x \nu_y e^{-i(\xi+\eta)h} \right], \end{aligned} \quad (4.6)$$

where ξ, η are the wave numbers along x -direction and y -direction, respectively; $i = \sqrt{-1}$, G is the amplification factor, and

$$C_M = h^2 \left[\frac{4}{9} + \frac{1}{9} c_\xi c_\eta + \frac{2}{9} (c_\xi + c_\eta) \right], \quad C_A = \frac{8}{3} - \frac{4}{3} c_\xi c_\eta - \frac{2}{3} (c_\xi + c_\eta),$$

$c_\xi = \cos(\xi h), c_\eta = \cos(\eta h)$. It is easy to check that $C_A \geq 0$ and $C_M > 0$. Take the absolute value of scheme (4.6), we get

$$|C_M + \varepsilon \Delta t C_A| |G| = C_M \left| (1 - \nu_x)(1 - \nu_y) + (1 - \nu_x) \nu_y e^{-i\eta h} + \nu_x (1 - \nu_y) e^{-i\xi h} + \nu_x \nu_y e^{-i(\xi+\eta)h} \right|.$$

Then we can obtain

$$|G| \leq \frac{C_M}{C_M + \varepsilon \Delta t C_A} \leq 1.$$

For $\nu_x > 1$ and/or $\nu_y > 1$, the proof is similar. □

4.1.2. Stability: on unstructured triangular meshes

We can prove a general result on an unstructured triangular mesh. For simplicity, we drop the superscripts of $u_{h,*}^n$ and u_h^n in this section.

Lemma 4.1. *Assume Δt is small enough. If y_j is in $\tau \in \mathcal{T}_h$, then*

$$|u_{h,*}(x_j) - u_h(x_j)| \lesssim \frac{\Delta t}{h} \sum_{k \in V(\tau)} |u_h(x_k)|, \tag{4.7}$$

where $V(\tau)$ is the indices set of vertices of the element τ .

Proof. Using the relationship (2.2) and the assumption that $\|b(x)\|_{L^\infty}$ is bounded, we know that $|y_j - x_j| = \mathcal{O}(\Delta t)$. Assume Δt is small enough, more precisely, y_j and x_j are in the same element τ (see Fig. 4.1.) It is easy to see that

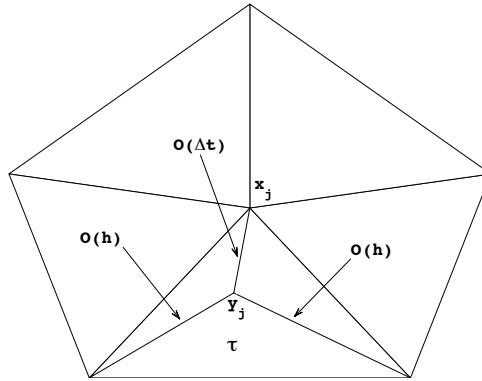


Fig. 4.1. The patch x_j and y_j belong to

$$|u_{h,*}(x_j) - u_h(x_j)| = \left| \sum_{k \in V(\tau)} (u_k \phi_k(y_j) - u_j \phi_k(y_j)) \right| \leq \sum_{k \in V(\tau), k \neq j} |u_k - u_j| \phi_k(y_j). \tag{4.8}$$

From Fig. 4.1, we can see that

$$\phi_k(y_j) \approx \frac{\Delta t \cdot h^{d-1}}{h^d} = \frac{\Delta t}{h}, \quad \text{for } k \neq j.$$

Then from (4.8), using the triangle inequality, we can complete the proof. □

Lemma 4.2. *Assume that the mesh \mathcal{T}_h is shape-regular and Δt is small enough. Then*

$$\|I_h u_{h,*}\| \leq \left(1 + C \frac{\Delta t}{h}\right) \|u_h\|, \tag{4.9}$$

where C is a constant, which is independent on Δt and h .

Proof. Using the triangle inequality, we obtain

$$\|I_h u_{h,*}\| \leq \|I_h u_{h,*} - u_h\| + \|u_h\| \lesssim \left(\sum_{\tau} h^d \|I_h u_{h,*} - u_h\|_{L^\infty(\tau)}^2 \right)^{\frac{1}{2}} + \|u_h\|, \tag{4.10}$$

here we use the shape-regularity of the mesh. Note that $I_h u_{h,*}$ and u_h are under the same mesh, and both of them are linear functions on each τ , so is $(I_h u_{h,*} - u_h)$, and the maximum

of $|I_h u_{h,*} - u_h|$ on element τ should be the value on one of the vertices of τ . Using Lemma 4.1, we have

$$\begin{aligned} \sum_{\tau} h^d \|I_h u_{h,*} - u_h\|_{L^\infty(\tau)}^2 &\leq \sum_{\tau} h^d \max_{k \in V(\tau)} |I_h u_{h,*}(x_k) - u_h(x_k)|^2 \\ &= \sum_{\tau} h^d \max_{k \in V(\tau)} |u_{h,*}(x_k) - u_h(x_k)|^2 \\ &\lesssim \sum_{\tau} h^d \left(\frac{\Delta t}{h}\right)^2 \sum_{k \in V(\tau)} |u_h(x_k)|^2 \lesssim \left(\frac{\Delta t}{h}\right)^2 \|u_h\|^2, \end{aligned}$$

which completes the proof. □

Theorem 4.3. *If the triangular mesh \mathcal{T}_h is shape-regular and Δt is small enough, then the finite element solution u_h of (4.2) satisfies*

$$\|u_h^{n+1}\| \leq (1 + C \frac{\Delta t}{h}) \|u_h^n\|, \tag{4.11}$$

where C is a constant independent of Δt and h .

Proof. Let $v_h = u_h^{n+1}$ in (4.2), and then using the Cauchy–Schwarz inequality, we have

$$\|u_h^{n+1}\| \leq \|I_h u_{h,*}^n\|. \tag{4.12}$$

By Lemma 4.2, we can obtain inequality (4.11). □

Remark 4.2. For the one- and two-dimensional structured grid case, we prove the unconditionally stable result that $\|u_h^{n+1}\| \leq \|u_h^n\|$; but for general unstructured meshes, we conjecture that the same result should be true, but we have not being able to prove it completely in Theorem 4.3. In Section 6, we verify this conjecture using numerical experiments.

4.1.3. Convergence

In this section, we analyze the accuracy of scheme (4.2) for the 1D constant-coefficient case, and show suboptimal convergence rate for Approach I.

First we analyze the truncation error of scheme (4.2) in the following lemma.

Lemma 4.3. *In the 1D constant-coefficient case, if $\nu < 1$, then the truncation error of scheme (4.2) is of $\mathcal{O}(\Delta t + h)$.*

Proof. In the 1D constant-coefficient case, for $\nu < 1$, by taking the Taylor expansion on (4.3) at (x_j, t^n) , and dividing the obtained equation by Δt , we can get that

$$u_t(x_j, t^n) + bu_x(x_j, t^n) - \varepsilon u_{xx}(x_j, t^n) + \frac{1}{2} \Delta t u_{tt}(x_j, t^n) - \frac{1}{2} bh u_{xx}(x_j, t^n) + \mathcal{O}(\Delta t + h^2) = 0. \tag{4.13}$$

Since $u(x, t)$ satisfies (2.1a), the truncation error of scheme (4.3) is

$$e_j^n = \frac{1}{2} (b^2 \Delta t - bh) u_{xx}(x_j, t^n) + \mathcal{O}(\Delta t + h^2). \tag{4.14}$$

The truncation error e_j^n is of order $\mathcal{O}(\Delta t + h)$. □

Combining the *stability* (Theorem 4.1) and *consistency* (Lemma 4.3), we obtain that the convergence rate of scheme (4.3) is $\mathcal{O}(\Delta t + h)$ for $\nu < 1$ by the Lax–Richtmyer equivalence theorem [22]. We use Problem 2.2 as a test example to check the convergence rate of this method. The numerical results are reported in Fig. 4.5 (left), in which we can see that the convergence rates for $\|u - \check{u}_h\|_{L^\infty(L^1)}$ and $\|u - \check{u}_h\|_{L^\infty(L^2)}$ are both first-order, which coincides with the expectation.

4.1.4. Numerical diffusion and accuracy of numerical quadratures

We now analyze numerical diffusion introduced by (4.2). For $\nu \leq 1$, we can obtain the modified equation of scheme (4.3):

$$u_t + bu_x - \varepsilon u_{xx} - \frac{1}{2}bh(1 - \nu)u_{xx} + \frac{1}{6}bh^2(1 - \nu)(1 - 2\nu)u_{xxx} + \mathcal{O}(h^3) = 0. \tag{4.15}$$

Remark 4.3. From (4.15), we can see that scheme (4.3) introduces a numerical diffusion term $-\frac{1}{2}bh(1 - \nu)u_{xx}$ and a dispersion term $\frac{1}{6}bh^2(1 - \nu)(1 - 2\nu)u_{xxx}$. If $\nu = 1$, the characteristic feet hit grid points exactly, i.e. $I_h u_{h,*}^n = u_{h,*}^n$, then the nodal interpolation approach (4.2) gives the exact RHS of (2.5), and the scheme (4.3) becomes the exact integration case as in Section 3.2. In this case, the coefficients of term u_{xx} and u_{xxx} are zero, and the equation (4.15) reduces to (3.2).

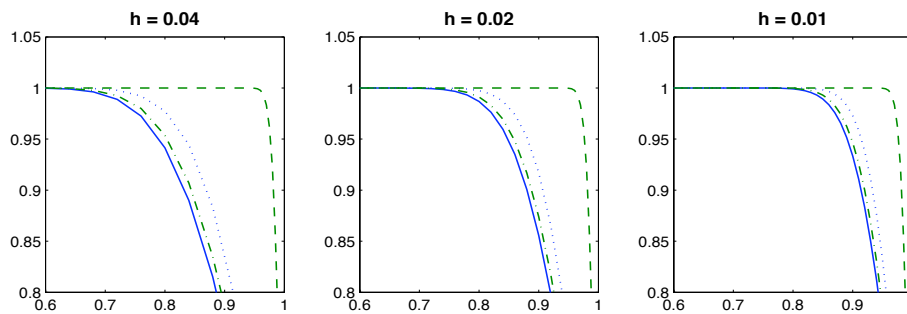


Fig. 4.2. Using Approach I to discretize Problem 2.1 ($\varepsilon = 10^{-4}$, $b = 1$, $T = 1$). Exact solution: dashed line; numerical solution: dotted line ($\Delta t = h/2$); dash-dot line ($\Delta t = h/4$); solid line ($\Delta t = h/8$).

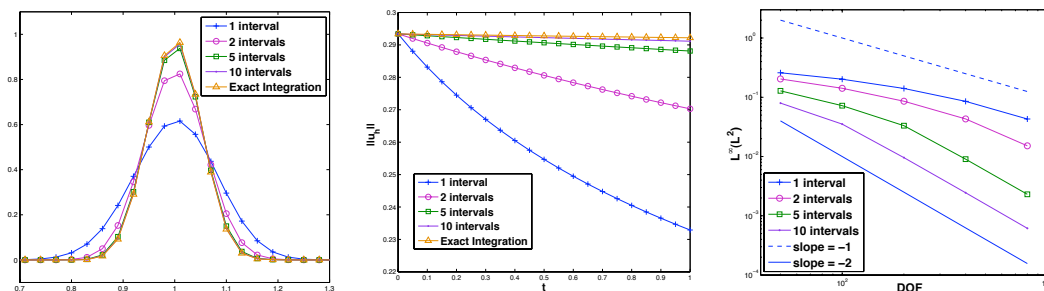


Fig. 4.3. Using modified Approach I (subelement interpolation) for Problem 2.2 ($\varepsilon = 0$, $\lambda = 1/20$, $\Delta t = 5 \times 10^{-2}$ and $T = 1$). (Left) the solutions obtained using different number of subintervals in each element. (Center) conservation of energy $\|u_h^n\|$. In these tests, the DOFs are fixed to be 100. (Right) convergence rate for $L^\infty(L^2)$ error.

Our numerical experiments (see Fig. 4.2) confirm this analysis. In Fig. 4.2, the effect of numerical diffusion increases, as Δt decreases for a fixed h . And it gets smaller when h gets smaller. Due to excessive numerical diffusion introduced by scheme (4.2), we do not see numerical oscillations.

Heuristically, we can expect better numerical solutions when using more accurate numerical quadratures for the RHS of (2.5). In Fig 4.2, we have seen that the interpolation approach introduces excessive numerical diffusion. One way to improve this method is to obtain more accurate the RHS of (2.5), by dividing each element into several smaller subelements (subintervals, in 1D), and then interpolate $u_{h,*}^n$ as a piecewise linear function in each subelement. Numerical experiments show that, when we use more subelements, we get less diffusive solutions. For example, we test this using Problem 2.2 with $\varepsilon = 0$. In Fig. 4.3, we can easily see that, the more subintervals we use for interpolation, the less numerical diffusion is introduced.

4.2. Approach II: Gauss quadratures

In this section, we discuss another standard integration technique — Gauss quadrature. We consider the scheme (2.5) with the two-point Gauss rule as an example:

$$(u_h^{n+1}, v_h) + \varepsilon \Delta t (\nabla u_h^{n+1}, \nabla v_h) = (u_{h,*}^n, v_h)_h, \tag{4.16}$$

where u_h^n is the finite element solution at t^n ; and $(\cdot, \cdot)_h$ means calculate this inner product with Gauss quadrature rule; for one-dimensional case, specifically, we use the two-point Gauss rule with the quadrature points $x_1 = \frac{3-\sqrt{3}}{6}$ and $x_2 = \frac{3+\sqrt{3}}{6}$ in $[0, 1]$, and the weights $\omega_1 = \omega_2 = 0.5$.

4.2.1. Stability

First, we refer to [12] for the stability of the ELM for the pure transport problem in one-dimension. For completeness, we give the main theorem in [12] as follows:

Theorem 4.4 ([12], Theorem 2.5) *If the RHS of the Eulerian–Lagrangian method, using piecewise linear elements on a uniform mesh, is approximated by a quadrature of the form*

$$\int_0^1 f(x) = \omega_0 f(0) + \sum_{k=1}^m \omega_k f(x_k) + \omega_{m+1} f(1), \tag{4.17}$$

where the weights $\omega_0, \dots, \omega_{m+1}$ and the quadrature points $0 < x_1 < \dots < x_m < 1$ are chosen to satisfy that the quadrature evaluates the integrations of quadratic polynomials exactly, then the method is unstable for $\nu \in (2\omega_{m+1}, 1 - x_m)$, if $2\omega_{m+1} < 1 - x_m$.

Remark 4.4. For the two-point Gauss quadrature rule, Theorem 4.4 shows an unstable region $\nu \in (0, \frac{3-\sqrt{3}}{6})$ for scheme (4.16). Following, we will show other unstable and stable regions.

Remark 4.5. In [12], the authors gave some examples of the quadratures which satisfy the condition of Theorem 4.4. For example, for the pure convection problem, any Gauss-Legendre quadrature that integrates quadratic polynomials exactly and has no quadrature point at $x = 1$ will lead to a method with a non-empty region of instability; all Gauss-Lobatto quadratures, except the vertex quadrature, lead to conditionally unstable ELM (see [12, Corollary 2.6]).

Now we show a stability result for the convection-diffusion problems with constant-coefficient in 1D, using the two-point Gauss quadrature rule. Under the assumption $\nu \leq 1$, we can write the numerical discretization in three different cases:

$$\text{Case I, } \nu \in \left(0, \frac{3 - \sqrt{3}}{6}\right); \quad \text{Case II, } \nu \in \left[\frac{3 - \sqrt{3}}{6}, \frac{3 + \sqrt{3}}{6}\right]; \quad \text{Case III, } \nu \in \left(\frac{3 + \sqrt{3}}{6}, 1\right].$$

Then scheme (4.16) can be written as

$$\text{Case I, } \left[1 + \left(\frac{1}{6} - \rho\right)\delta^2\right] u_j^{n+1} = \left(\frac{1}{6} + \frac{1}{2}\nu\right) u_{j-1}^n + \frac{2}{3}u_j^n + \left(\frac{1}{6} - \frac{1}{2}\nu\right) u_{j+1}^n, \tag{4.18}$$

$$\begin{aligned} \text{Case II, } \left[1 + \left(\frac{1}{6} - \rho\right)\delta^2\right] u_j^{n+1} &= \left(\frac{\sqrt{3}-2}{12} + \frac{3-\sqrt{3}}{12}\nu\right) u_{j-2}^n + \left(\frac{5-2\sqrt{3}}{12} + \frac{1+\sqrt{3}}{4}\nu\right) u_{j-1}^n \\ &+ \left(\frac{8+\sqrt{3}}{12} - \frac{1+\sqrt{3}}{4}\nu\right) u_j^n + \left(\frac{1}{12} - \frac{3-\sqrt{3}}{12}\nu\right) u_{j+1}^n, \end{aligned} \tag{4.19}$$

$$\text{Case III, } \left[1 + \left(\frac{1}{6} - \rho\right)\delta^2\right] u_j^{n+1} = \left(-\frac{1}{3} + \frac{1}{2}\nu\right) u_{j-2}^n + \frac{2}{3}u_{j-1}^n + \left(\frac{2}{3} - \frac{1}{2}\nu\right) u_j^n, \tag{4.20}$$

and we have the following stability result.

Theorem 4.5. *In the 1D constant-coefficient case, when we use the two-point Gauss quadrature rule for scheme (4.16). If $\nu \leq 1$, then the stable region for scheme (4.16) is*

$$\nu \in \begin{cases} (0, \sqrt{2\rho}) \cup \left[\frac{1}{2} - \rho_1, \frac{1}{2} + \rho_1\right] \cup (1 - \sqrt{2\rho}, 1], & \text{for } \rho \in \left[0, \frac{2-\sqrt{3}}{12}\right) \\ (0, 1], & \text{for } \rho \in \left[\frac{2-\sqrt{3}}{12}, \infty\right), \end{cases} \tag{4.21}$$

where $\rho_1 = \frac{\sqrt{-3+2\sqrt{3}+24\rho}}{2\sqrt{3}}$.

Proof. Apply the discrete Fourier transformation on (4.18), (4.19) and (4.20) we have

$$\text{Case I, } \left(1 - \frac{2}{3}s^2 + 4\rho s^2\right) G = 1 - \frac{2}{3}s^2 + 2scvi,$$

$$\begin{aligned} \text{Case II, } \left(1 - \frac{2}{3}s^2 + 4\rho s^2\right) G &= 1 + \left(\frac{\sqrt{3}-3}{3} - \frac{2\sqrt{3}}{3}\nu\right) s^2 - \left(\frac{2\sqrt{3}-4}{3} + \frac{6-2\sqrt{3}}{3}\nu\right) s^2 c^2 \\ &+ i \left[\left(\frac{2\sqrt{3}-4}{3} + \frac{6-2\sqrt{3}}{3}\nu\right) s^3 c - 2scv\right], \end{aligned}$$

$$\text{Case III, } \left(1 - \frac{2}{3}s^2 + 4\rho s^2\right) G = 1 + \frac{4}{3}s^2(1 - 2s^2) - 4s^2\nu(1 - s^2) + i \left[4s^3c\nu - \frac{8}{3}s^3c - 2scv\right],$$

where $i = \sqrt{-1}$, $s = \sin(\xi h/2)$, $c = \cos(\xi h/2)$, ξ is the wave number, and G is the amplification factor.

In order to make $|G|^2 \leq 1$, we need, $\forall s \in [-1, 1]$,

$$\text{Case I, } \left(\frac{1}{4}\nu^2 + \rho^2 - \frac{1}{3}\rho\right) s^2 \geq \frac{1}{4}\nu^2 - \frac{1}{2}\rho,$$

$$\begin{aligned} \text{Case II, } \left(\frac{8(3-\sqrt{3})}{3}(\nu^2 - \nu) + 16\rho^2 - \frac{16}{3}\rho + \frac{2(12-5\sqrt{3})}{9}\right) s^2 \\ - \frac{8(2-\sqrt{3})}{3}(\nu^2 - \nu + \frac{1}{6})s^4 \geq 4\nu^2 - 4\nu - 8\rho + \frac{2(3-\sqrt{3})}{3}, \end{aligned}$$

$$\text{Case III, } \left(4(1-\nu)^2 + 16\rho^2 - \frac{16}{3}\rho\right) s^2 \geq 4(1-\nu)^2 - 8\rho.$$

We complete the proof by solving these inequalities and some simplifications. □

Remark 4.6. We summarize some observations from Theorem 4.5: For $\nu \leq 1$,

1. scheme (4.16) is stable, if $\Delta t \geq \frac{2 - \sqrt{3} h^2}{12 \varepsilon}$, or $\Delta t < \frac{2 - \sqrt{3} h^2}{12 \varepsilon}$ and $\Delta t < \frac{2\varepsilon}{b^2}$ are satisfied.
2. scheme (4.16) is unconditionally stable, if $h \leq \sqrt{24(2 + \sqrt{3})} \frac{\varepsilon}{b} \approx 9.464 \frac{\varepsilon}{b}$ is satisfied.

Remark 4.7. For the pure transport problem ($\varepsilon = 0$), [12] showed that $\nu \in (0, \frac{3-\sqrt{3}}{6})$ is an unstable region for scheme (4.16); and Theorem 4.5 gives the stable region

$$\nu \in \left[\frac{3 - \sqrt{6\sqrt{3} - 9}}{6}, \frac{3 + \sqrt{6\sqrt{3} - 9}}{6} \right].$$

We test the results in Theorem 4.5 using Problem 2.1 and report the results in Fig. 4.4. When $\Delta t = \frac{1}{400}$ and $\Delta t = \frac{1}{120}$, ν does not satisfy (4.21); in these two cases, the solutions are unstable. When $\Delta t = \frac{1}{200}$ and $\Delta t = \frac{1}{110}$, ν is in the stable region and we obtain stable solutions as expected.

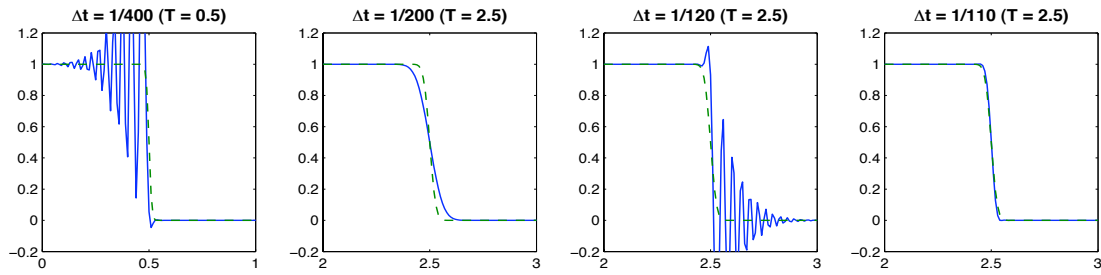


Fig. 4.4. Using Approach II for Problem 2.1, we use the two-point Gauss quadrature ($\varepsilon = 10^{-4}$, $b = 1$, $h = 10^{-2}$).

Remark 4.8. For the two unstable cases shown in Fig. 4.4, we can calculate the group velocity¹⁾ for the wave number ξ (see [23] for the details). For the case $\Delta t = \frac{1}{400}$, the group velocity is $b - 1.78 \times 10^{-6} \xi^2$, which means that the high-frequency components of the numerical solution travel slower than the low-frequency components. Hence, this is essentially why numerical oscillations appear behind the shock. For the case $\Delta t = \frac{1}{120}$, the group velocity is $b + 1.85 \times 10^{-7} \xi^2$, which means that the high-frequency components of the numerical solution travel faster than the low-frequency components and numerical oscillations appear in front of the shock.

4.2.2. Convergence

In this section, we show the consistency of scheme (4.16) with the two-point Gauss quadrature rule for the 1D constant-coefficient convection-diffusion equation (2.1).

Lemma 4.4. *In the 1D constant-coefficient case, if $\nu \leq 1$, the truncation error of scheme (4.16) is of order $\mathcal{O}(\Delta t + h^2)$, if $\nu \in (0, \frac{3-\sqrt{3}}{6})$, and $\mathcal{O}(\Delta t + h + \frac{h^2}{\Delta t})$, if $\nu \in [\frac{3-\sqrt{3}}{6}, 1]$, respectively.*

¹⁾ Suppose the solution of (2.1a) has the form $u(x, t) = e^{i(\omega t - \xi x)}$, $i = \sqrt{-1}$, for each real wave number ξ , assume there is a corresponding real frequency $\omega(\xi)$, then the group velocity is defined as $\frac{d\omega(\xi)}{d\xi}$.

Proof. For simplicity, we take Case I for example. Take the Taylor expansion on (4.18) at (x_j, t^n) , we can get that

$$u_t + bu_x - \varepsilon u_{xx} + \frac{1}{2}\Delta t u_{tt} + \frac{1}{6}\Delta t^2 u_{ttt} + \left(\frac{1}{6}h^2 - \varepsilon\Delta t\right)u_{txx} + \frac{1}{6}bh^2 u_{xxx} + \frac{1}{24}\Delta t^3 u_{tttt} + \left(\frac{1}{12}\Delta th^2 - \frac{1}{2}\varepsilon\Delta t^2\right)u_{ttxx} - \frac{1}{12}\varepsilon h^2 u_{xxxx}|_{(x_j, t^n)} + h.o.t. = 0.$$

Since $u(x, t)$ satisfies (2.1a), we get that the truncation error of scheme (4.16) for Case I is

$$\begin{aligned} e_1^n &= \frac{1}{2}\Delta t u_{tt} + \frac{1}{6}\Delta t^2 u_{ttt} + \left(\frac{1}{6}h^2 - \varepsilon\Delta t\right)u_{txx} + \frac{1}{6}bh^2 u_{xxx} \\ &\quad + \frac{1}{24}\Delta t^3 u_{tttt} + \left(\frac{1}{12}\Delta th^2 - \frac{1}{2}\varepsilon\Delta t^2\right)u_{ttxx} - \frac{1}{12}\varepsilon h^2 u_{xxxx}|_{(x_j, t^n)} + h.o.t. \\ &= \frac{1}{2}b^2\Delta t u_{xx} + \left(\frac{1}{12}\varepsilon h^2 - \frac{1}{2}\varepsilon^2\Delta t\right)u_{xxxx}|_{(x_j, t^n)} + h.o.t., \end{aligned}$$

which completes the proof for Case I. For Case II and III, the proof is similar. □

Combining Theorem 4.5 and Lemma 4.4, we can get the convergence result for scheme (4.16). For the 1D constant-coefficient case, with $\nu < 1$, scheme (4.16) converges with order

$$\begin{cases} \mathcal{O}(\Delta t + h^2), & \nu \in \left(0, \min\left\{\sqrt{2\rho}, \frac{3-\sqrt{3}}{6}\right\}\right), \\ \mathcal{O}(\Delta t + h + \frac{h^2}{\Delta t}), & \nu \in \left[\max\left\{\frac{1}{2} - \rho_1, \frac{3-\sqrt{3}}{6}\right\}, \min\left\{\frac{1}{2} + \rho_1, \frac{3+\sqrt{3}}{6}\right\}\right] \\ & \cup \left(\max\left\{1 - \sqrt{2\rho}, \frac{3+\sqrt{3}}{6}\right\}, 1\right). \end{cases}$$

We observe that scheme (4.16) converges with the optimal rate $\mathcal{O}(\Delta t + h^2)$, when

$$\Delta t \in \left(0, \min\left\{2\varepsilon, \frac{3-\sqrt{3}}{6}h\right\}\right).$$

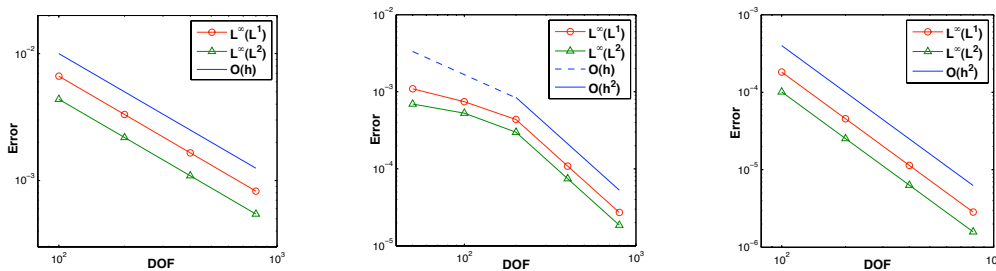


Fig. 4.5. Convergence rates of the linear finite element ELM with Approach I (left, $\Delta t = 10^{-6}$) and Approach II (middle and right) for Problem 2.2 ($\varepsilon = 10^{-1}, b = 1, \lambda = 1/10$). For Approach I, both $\|u - u_h\|_{L^\infty(L^1)}$ and $\|u - u_h\|_{L^\infty(L^2)}$ are of order $\mathcal{O}(h)$. For Approach II (middle), we divide Δt by 4, and divide h by 2 for each test; when Δt is relatively large, we get first-order convergence rate, and when Δt is small enough, we get second-order convergence rate. For Approach II (right), if we fix $\Delta t = 10^{-5}$, we get second-order convergence rate for both $\|\cdot\|_{L^\infty(L^1)}$ and $\|\cdot\|_{L^\infty(L^2)}$ error w.r.t. h .

For $\nu \in [\frac{3-\sqrt{3}}{6}, \frac{3+\sqrt{3}}{6}]$ and $\nu \in (\frac{3+\sqrt{3}}{6}, 1)$, there is an $h^2/\Delta t$ term in the error. Since Δt is relatively large and the ratio of $h/\Delta t$ is bounded, the total error is $\mathcal{O}(\Delta t + h)$. We take

Problem 2.2 for example. We divide Δt by 4, and divide h by 2 for each test to get the convergence rate and report the results in Fig. 4.5 (middle). We can see that, when Δt is large, we get first-order convergence; and when Δt gets smaller, we get second-order convergence. In Fig. 4.5 (right), we fix $\Delta t = 10^{-5}$, which is small enough compared with h ; in this case, we get the second-order convergence rate for the error in both $\|\cdot\|_{L^\infty(L^1)}$ and $\|\cdot\|_{L^\infty(L^2)}$ norms.

From Fig. 4.6, we can see that the two-point Gauss quadrature approach introduces small numerical diffusion compared with the interpolation approach. This is consistent with our expectation in Remark 3.1. Furthermore, as shown in Section 4.1.4, using exact integrations gives a numerical solution with very little numerical diffusion. These observations suggest that, when more accurate integrations are employed for the RHS in (2.5), less numerical diffusion is introduced to the numerical solution.



Fig. 4.6. Comparison of the numerical diffusion introduced by interpolation, two-point Gauss quadrature and exact integration scheme for Problem 2.1 (left, $\varepsilon = 10^{-3}, b = 1, h = 1.3 \times 10^{-2}, \Delta t = 5 \times 10^{-3}, T = 1.0$) and Problem 2.2 (right, $\varepsilon = 10^{-6}, b = 1, h = 1.5 \times 10^{-2}, \Delta t = 5 \times 10^{-3}, T = 0.5$). We zoomed in to the interested region. Solid line: exact solution; dashed line: numerical solution with exact integrations; dotted line: numerical solution with Gauss quadratures; dash-dot line: numerical solution with interpolation.

To conclude this section, we summarize the advantages and disadvantages for using both exact and inexact integrations in Table 4.1:

Table 4.1: Comparison of exact and inexact integrations

Exact integration	Approach I	Approach II
Unconditionally stable	Unconditionally stable	Conditionally stable
Little numerical diffusion	Excessive numerical diffusion	Small numerical diffusion
Optimal convergence rate	Suboptimal convergence rate	Optimal convergence rate
Little oscillation	No oscillation	Some oscillations

5. Adaptive Eulerian–Lagrangian Method

We now give two simple observations:

- In Remark 4.3, we show that the numerical diffusion term of (4.3) is $\frac{1}{2}bh(1 - \nu)u_{xx}$. The adaptive procedure puts more grid points inside (and close to) the singularity, where u_{xx} is large, and gives very small h locally and could reduce the numerical diffusion substantially.

- Theorem 4.5 implies that, when h is small enough compared with ε , more precisely, when $h \leq \sqrt{24(2 + \sqrt{3})} \frac{\varepsilon}{b}$, scheme (4.16) is always stable for $\nu \leq 1$.

These make us believe that mesh adaptivity can cure the problems caused by inexact integrations (cf. Table 4.1).

5.1. Adaptive algorithm

A posteriori error analysis and spatial adaptive algorithms have been discussed extensively; see [24] for details. We adopt the adaptive strategy for the time-dependent problems described in [25] (but with fixed time-step size Δt); see Algorithm 5.1.

Algorithm 5.1 Adaptive Mesh Refinement—One Time-step

Given tolerance tol , time-step size Δt , and the solution u_h^n on grid \mathcal{T}_h^n ;
 $\mathcal{T}_h^{n+1} := \mathcal{T}_h^n$;
 use ELM to solve for u_h^{n+1} by tracing back the characteristic feet on \mathcal{T}_h^{n+1} ;
 compute an error estimator η on \mathcal{T}_h^{n+1} ;
while $\eta > tol$ **do**
 mark elements for refinement or coarsening;
 if elements are marked **then**
 adapt mesh \mathcal{T}_h^{n+1} producing a modified \mathcal{T}_h^{n+1} ; and interpolate u_h^n onto the new \mathcal{T}_h^{n+1} ;
 use ELM to solve for u_h^{n+1} by tracing back the characteristic feet on \mathcal{T}_h^{n+1} ;
 compute error estimator η on \mathcal{T}_h^{n+1} ;
 end if
end while

We use the so-called *guaranteed error reduction* strategy in [25] and the spatial error estimators proposed in [17]. Our implementation is based on a Matlab adaptive finite element package, AFEM@matlab [26].

5.2. Adaptive ELM with nodal interpolation

As we have pointed out before, Approach I is unconditionally stable and does not introduce any nonphysical oscillation. We expect space adaptivity could preserve these advantages. We use Problem 2.1 to test the effects of adaptivity for Approach I. Fig 5.1 shows that the adaptive mesh refinement can reduce the numerical diffusion substantially. Fig. 5.2 (left), where the x -label is the average degrees of freedom of the adaptive procedure, shows that adaptivity help us to improve the convergence rate to 1.5 asymptotically. Since we use the linear nodal interpolation to approximate $u_{h,*}^n$, which belongs to $H^{1.5-\mu}(\Omega)$, 1.5 is the best convergence rate we can expect.

As we mentioned in Section 4.1.3, when we use subelement interpolations, we can reduce numerical diffusion. Now we show the effects of the subelement interpolation on adaptive meshes. To get rid of the influence of the adaptive procedure, we use the same grids obtained by adaptive mesh refinements with exact integrations. The results are reported in Fig. 5.3. We can see that the more subintervals we use in each element, the less diffusive solution we obtain. Fig. 5.3 (right) plot the behavior of $\|u_h\|$ with the time marching. When we use more subintervals for interpolation, $\|u_h\|$ damps slightly, which means only small numerical diffusion is introduced.

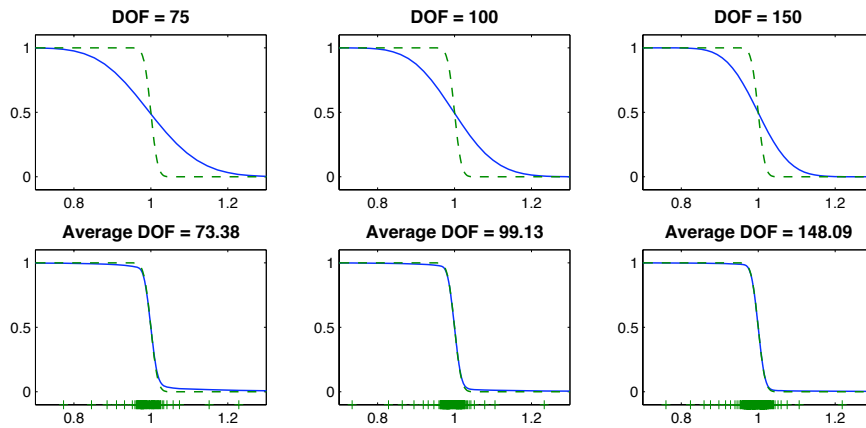


Fig. 5.1. Using Approach I to discretize Problem 2.1 ($\varepsilon = 10^{-4}$, $\Delta t = 5 \times 10^{-3}$, $b = 1$, $T = 1.0$.) Comparison between the uniform (upper) and adaptive (lower) grid; solid line: numerical solution; dashed line: exact solution.

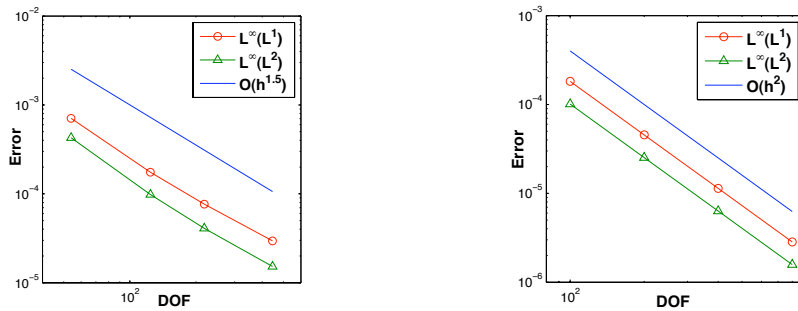


Fig. 5.2. Using Approach I (left) and Approach II (right) with the adaptive mesh refinement to discretize Problem 2.2 ($\varepsilon = 10^{-1}$, $b = 1$, $\lambda = 1/10$, $\Delta t = 10^{-6}$.) For both $\|u - u_h\|_{L^\infty(L^1)}$ and $\|u - u_h\|_{L^\infty(L^2)}$, we get convergence rate $\mathcal{O}(h^{1.5})$ for Approach I, and $\mathcal{O}(h^2)$ for Approach II.

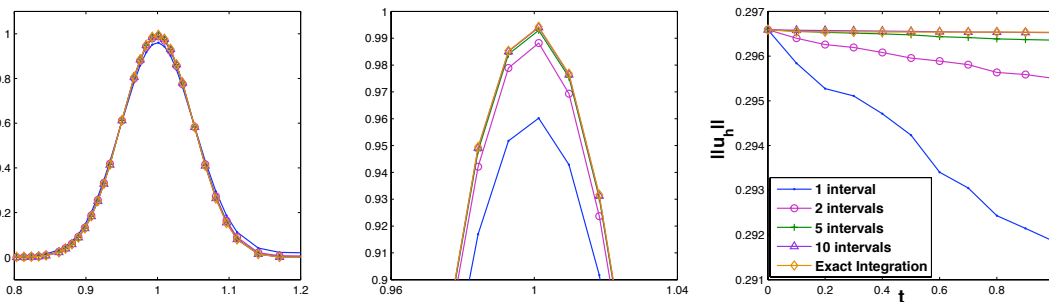


Fig. 5.3. Using modified Approach I (subelement interpolation) for Problem 2.2 ($\varepsilon = 0$, $\lambda = 1/20$, $\Delta t = 0.1$ and $T = 1$). Left: the solutions obtained using different number of subintervals in each element. Middle: zoom in. Right: conservation of energy. In these tests, the average DOFs are all 40.

5.3. Adaptive ELM with the two-point Gauss quadrature

In Section 4.2, we have seen that one of the drawbacks for using the two-point Gauss quadrature is that it is conditionally unstable. On the other hand, Remark 4.6 tell us, when $h \leq$

$\sqrt{24(2 + \sqrt{3})} \frac{\varepsilon}{b}$, scheme (4.16) is always stable. When we employ adaptive mesh refinements, we get smaller h near singularities, which makes h satisfy the stable condition locally. So we expect that adaptive mesh refinement can improve stability also.

We use Problem 2.1 to test this, the results are reported in Fig. 5.4, which confirm our expectation. In Section 6.3, we use 2D tests to confirm this. Moreover, Fig. 5.2 (right) shows the second order convergence rate.

Introducing numerical oscillations is another drawback of Approach II (see Fig. 5.4). It is well-known that numerical oscillations can be eliminated by making the discrete linear system an M-matrix, which guarantees the discrete maximum principle; see [21] for details.

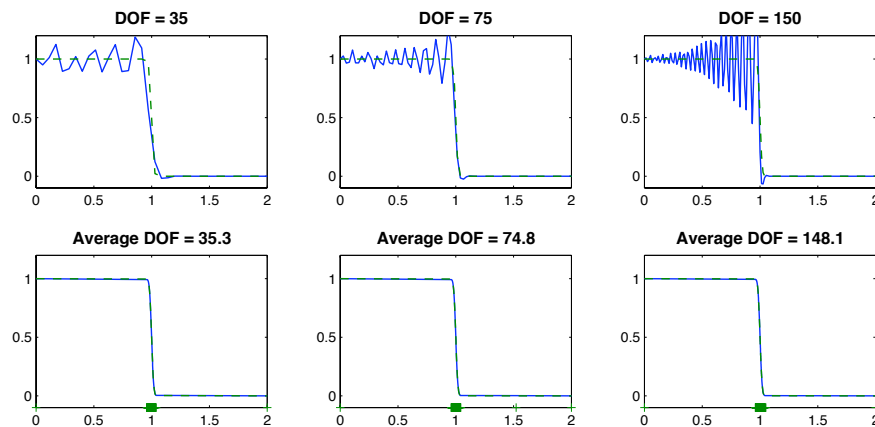


Fig. 5.4. Using Approach II to discretize Problem 2.1 ($\varepsilon = 10^{-4}$, $\Delta t = 10^{-3}$, $b = 1$ and $T = 1.0$.) Comparison between the uniform (upper) and adaptive (lower) grid; solid line: numerical solution; dashed line: exact solution.

In Remark 3.3, we have given the diagonal and off-diagonal entries of the discrete system of (2.5). When we use the adaptive mesh refinement, mesh size inside or close to the singularity is small due to the adaptive procedure. Hence, if x_j is inside or near the singularity, the off-diagonal entries K_{jk} are non-positive, the diagonal entries are all positive, which satisfies the definition of M-matrix. Adaptivity makes the corresponding rows of the coefficient matrix satisfy the M-matrix conditions, which can dismiss numerical oscillations substantially.

At the end of this section, we point out that, although adaptivity can help Approach I to reduce the numerical diffusion, the convergence rate is still suboptimal. Hence, Approach II is preferred, when it is stable. In the next section, we will mainly use Approach II for the 2D numerical experiments.

6. Numerical Experiments

In this section, we will show the numerical experiments in two-dimension, with piecewise linear continuous element on a shape-regular triangular mesh \mathcal{T}_h .

6.1. 2D test problems

First, we state five test examples:

Problem 6.1. *This example is a hump changing its height in the course of the time (cf. [27]). Given the homogenous initial condition and the velocity filed $b = (2, 3)^T$, we choose the source term such that the exact solution has the form*

$$u(x, y, t) = 16 \sin(\pi t) x(1-x)y(1-y) \left\{ \frac{1}{2} + \frac{1}{\pi} \arctan \left[\frac{2}{\sqrt{\varepsilon}} (0.25^2 - (x-0.5)^2 - (y-0.5)^2) \right] \right\},$$

the computational domain is $[0, 1] \times [0, 1]$ in \mathbb{R}^2 .

Problem 6.2. *The second test problem is the benchmark Gaussian-cone problem (cf. [28]). Given the velocity field $b = (y, -x)^T$ and the initial condition*

$$u(x, y, 0) = \exp \{ -[(x-x_0)^2 + (y-y_0)^2]/(2\lambda^2) \}.$$

The exact solution is

$$u(x, y, t) = \frac{\lambda^2}{\lambda^2 + 2\varepsilon t} \exp \{ -[\hat{x}^2 + \hat{y}^2]/(2\lambda^2 + 4\varepsilon t) \},$$

where $\hat{x} = x - x_0 \cos(t) - y_0 \sin(t)$, $\hat{y} = y + x_0 \sin(t) - y_0 \cos(t)$, $\lambda = \frac{1}{8}$, and $(x_0, y_0) = (-\frac{1}{2}, 0)$. The computational domain is $[0, 1] \times [0, 1]$ in \mathbb{R}^2 .

The third and fourth tests are generalizations of the one-dimensional problem, Problem 2.1.

Problem 6.3. *Given the velocity field $b = (1, 0)^T$, and the initial condition*

$$u(x, y, 0) = \begin{cases} 1, & \text{if } x < 0.2, \\ 0, & \text{otherwise,} \end{cases}$$

then the exact solution is

$$u(x, y, t) = \frac{1}{2} \left\{ \operatorname{erfc} \left(\frac{x-t}{2\sqrt{\varepsilon t}} \right) + \exp \left(\frac{x}{\varepsilon} \right) \operatorname{erfc} \left(\frac{x+t}{2\sqrt{\varepsilon t}} \right) \right\},$$

the computational domain is $[0, 1] \times [0, 1]$ in \mathbb{R}^2 .

Problem 6.4. *Given the velocity field $b = (1, 1)^T$, and the initial condition as*

$$u(x, y, 0) = \begin{cases} 1, & \text{if } x < 0.2 \text{ and } y < 0.2, \\ 0, & \text{otherwise.} \end{cases}$$

The exact solution is

$$u(x, y, t) = \frac{1}{4} \left\{ \operatorname{erfc} \left(\frac{x-t}{2\sqrt{\varepsilon t}} \right) + \exp \left(\frac{x}{\varepsilon} \right) \operatorname{erfc} \left(\frac{x+t}{2\sqrt{\varepsilon t}} \right) \right\} \left\{ \operatorname{erfc} \left(\frac{y-t}{2\sqrt{\varepsilon t}} \right) + \exp \left(\frac{y}{\varepsilon} \right) \operatorname{erfc} \left(\frac{y+t}{2\sqrt{\varepsilon t}} \right) \right\},$$

and the computational domain is $[0, 1] \times [0, 1]$ in \mathbb{R}^2 .

The last test is the so-called rotating cylinder problem (see [17, Example 1].)

Problem 6.5. *Given the velocity field $b = -2\pi(2y-1, 1-2x)^T$, and the initial condition as*

$$u(x, y, 0) = \begin{cases} 1, & \text{if } (2x-1/2)^2 + (2y-1)^2 \leq 1/4, \\ 0, & \text{otherwise,} \end{cases}$$

and the computational domain is $[0, 1] \times [0, 1]$ in \mathbb{R}^2 .

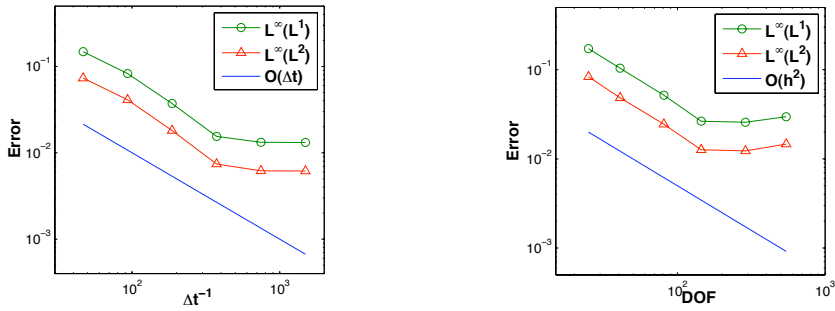


Fig. 6.1. Using Approach II to discretize Problem 6.1 ($\varepsilon = 10^{-1}$), with three-point Gauss quadrature rule, under the structure grid; we fix the DOF = 289 (left), halve Δt for each test; and we fix $\Delta t = 4 \times 10^{-3}$ (right), double the DOF for each test.

6.2. Convergence tests

In this section, we test the convergence rate for the adaptive ELM with Gauss quadratures. First, we fix Δt and DOF, respectively, to test the convergence behavior with respect to each of them. The results are reported in Fig. 6.1: When we fix the DOF and halve Δt in each test (Fig. 6.1 (left)), if Δt is relatively large, we get first-order convergence for both $\|u - u_h\|_{L^\infty(L^1)}$ and $\|u - u_h\|_{L^\infty(L^2)}$ w.r.t. Δt ; if Δt is small enough (at the turning point, $\Delta t = 2.7 \times 10^{-3}$), the space error dominates the total error. When we fix Δt and double the DOF in each test (Fig. 6.1 (right)), if DOF is small, we get second-order convergence rates for both $\|u - u_h\|_{L^\infty(L^1)}$ and $\|u - u_h\|_{L^\infty(L^2)}$; if DOF is large (at the turning point, DOF = 145), the temporal error dominates the total error. Roughly speaking, the magnitude of the spatial and the temporal error are close at the turning point. If the error is in the form $C_t \Delta t + C_h h^2$ (i.e., $C_t \Delta t + C_h / \text{DOF}$), at the turning point, $C_h / C_t \approx 0.78$, for the fixed- Δt case; and $C_h / C_t \approx 0.58$, for the fixed-DOF case.

This observation tells us that, when $\Delta t / h^2 (= \Delta t \cdot \text{DOF}) \approx 1$, the spatial error and temporal error are close to each other. We design the following tests to show the convergence rate for Problem 6.1: starting from the structured (Fig. 6.2 (left)) and unstructured (Fig. 6.2 (right)) initial grid, respectively, perform uniform bisections (double the DOF) and halve Δt in each test; this way, in each test, we have $\Delta t \cdot \text{DOF} \approx 1$. We obtain second order convergence rates for both $\|\cdot\|_{L^\infty(L^1)}$ and $\|\cdot\|_{L^\infty(L^2)}$ error.

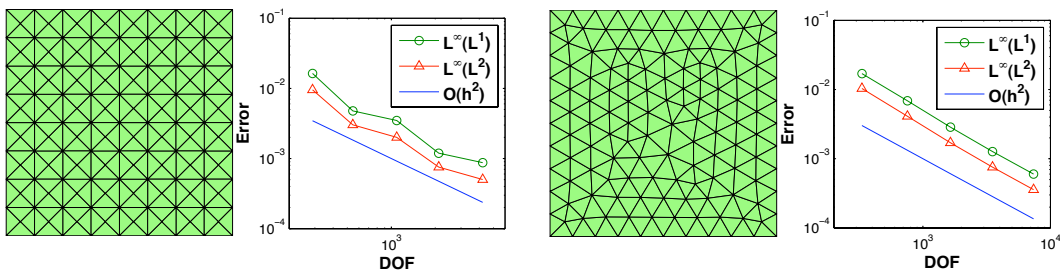


Fig. 6.2. Using Approach II to discretize Problem 6.1 ($\varepsilon = 10^{-1}$), with the three-point Gauss quadrature rule, under the structured grid (left) and unstructured grid (right). We get second-order convergence for both $\|\cdot\|_{L^\infty(L^1)}$ and $\|\cdot\|_{L^\infty(L^2)}$ error.

6.3. Effects of adaptivity on stability

In this section, we discuss the effects of adaptivity on stability of the ELM with Gauss quadrature. In this subsection, for the RHS of (2.5), we use the 3-point Gauss quadrature rule. Figs. 6.3, 6.4, 6.5, and 6.6 show the numerical solutions for Problems 6.1, 6.2, 6.3 and 6.4, respectively. We find that, when we use uniform grids, oscillations pollute most of the computational domain if the grids are not fine enough; the adaptive mesh refinement helps to dismiss the oscillations with nearly the same spatial degrees of freedom as the corresponding uniform grids.

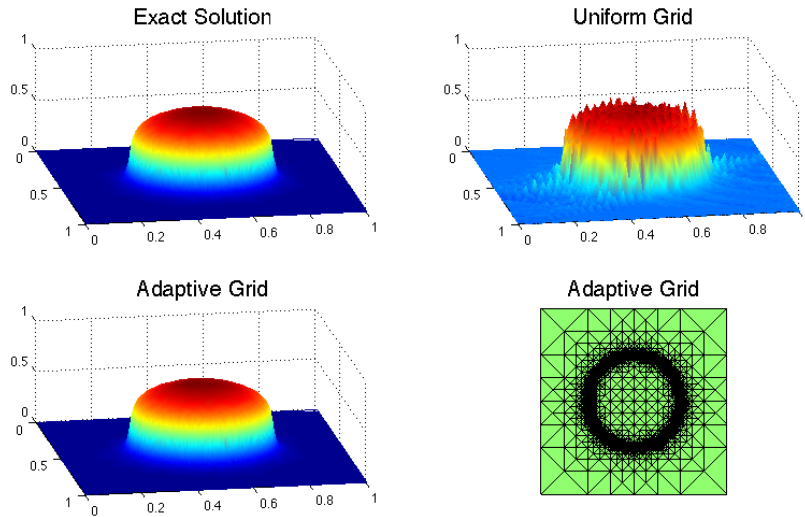


Fig. 6.3. Using Approach II to discretize Problem 6.1 ($\varepsilon = 10^{-4}, \Delta t = 10^{-4}$ and $T = 0.25$.) For the uniform grid (upper right), DOF is 4225; For the adaptive grid (lower left), the average DOF is 4250. The lower right figure is the adaptive grid at the final time.

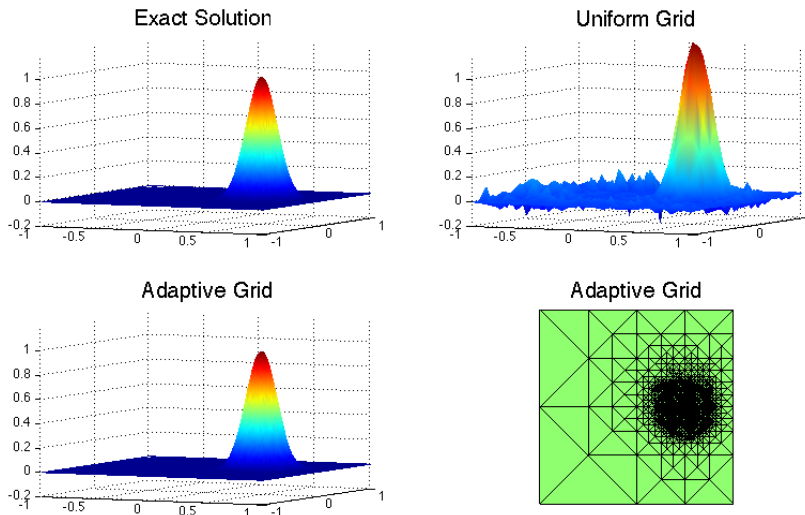


Fig. 6.4. Using Approach II to discretize Problem 6.2 ($\varepsilon = 10^{-4}, \Delta t = 10^{-2}$ and $T = \pi$.) For the uniform grid (upper right), DOF is 1089; For the adaptive grid (lower left), the average DOF is 1153. The lower-right figure is the adaptive grid at the final time.

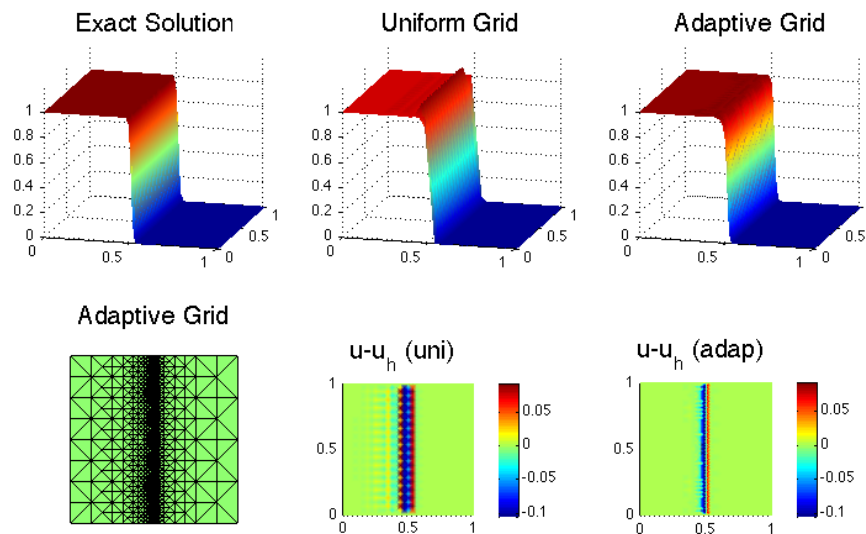


Fig. 6.5. Using Approach II to discretize Problem 6.3 ($\varepsilon = 10^{-4}$, $\Delta t = 10^{-4}$ and $T = 0.5$.) For the uniform grid (upper middle), DOF is 1089; For the adaptive grid (upper right), the average DOF is 1031. The lower-left figure is the adaptive grid at the final time. The lower-middle and -right subfigures are $u - u_h$ error.

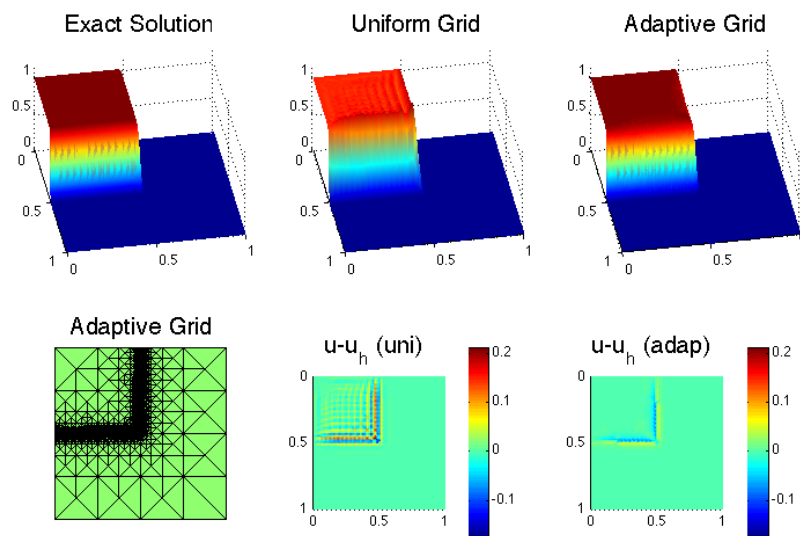


Fig. 6.6. Using Approach II to discretize Problem 6.4 ($\varepsilon = 10^{-4}$, $\Delta t = 10^{-4}$ and $T = 0.5$.) For the uniform grid (upper middle), DOF is 4225; For the adaptive grid (upper right), the average DOF is 4106. The lower-left figure is the adaptive grid at the final time. The lower-middle and -right subfigures are $u - u_h$ error.

Fig. 6.7 reports the long-term behavior of $\|u_h^n\|$ obtained by Approach I on both uniform and adaptive grid for Problem 6.2; and the experiments confirm the stability result, $\|u_h^{n+1}\| \leq \|u_h^n\|$, aforesated in Remark 4.2. This example also indicates that, using adaptive mesh refinement, the method is much less diffusive.

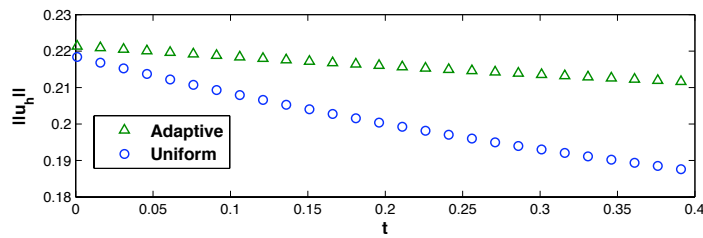


Fig. 6.7. Long-term behavior of $\|u_h\|$ using Approach I for Problem 6.2 ($\varepsilon = 10^{-6}$, $\lambda = 1/8$, $\Delta t = 10^{-3}$, $T = \pi/8$) on uniform grids (DOF = 2113) and on adaptive grids (average DOF = 2222.)

6.4. Effects of accuracy of integrations on numerical diffusion and oscillations

In this section, we test the effects of accuracy of the integrations on numerical diffusion and oscillations. Numerical experiments in Section 4.1.4 suggested that more accurate numerical quadratures yield less diffusive ELM schemes. This is confirmed by our numerical tests in 2D on adaptive meshes as well. The numerical results reported in Figs. 6.8 and 6.9 are for Problem 6.5. In these tests, we use the same meshes obtained by the 33-point Gauss quadrature to get rid of the influence of adaptive mesh refinement procedure. We observe that when interpolation approach is used, numerical diffusion is relatively large; see Fig. 6.9 (upper). When the 12-point Gauss quadrature is used, the solution is less diffusive but oscillatory; see Fig. 6.9 (lower). If we use more quadrature points (33-point Gauss points), we can get a much better approximation with very little numerical diffusion and oscillations; see Fig. 6.8.

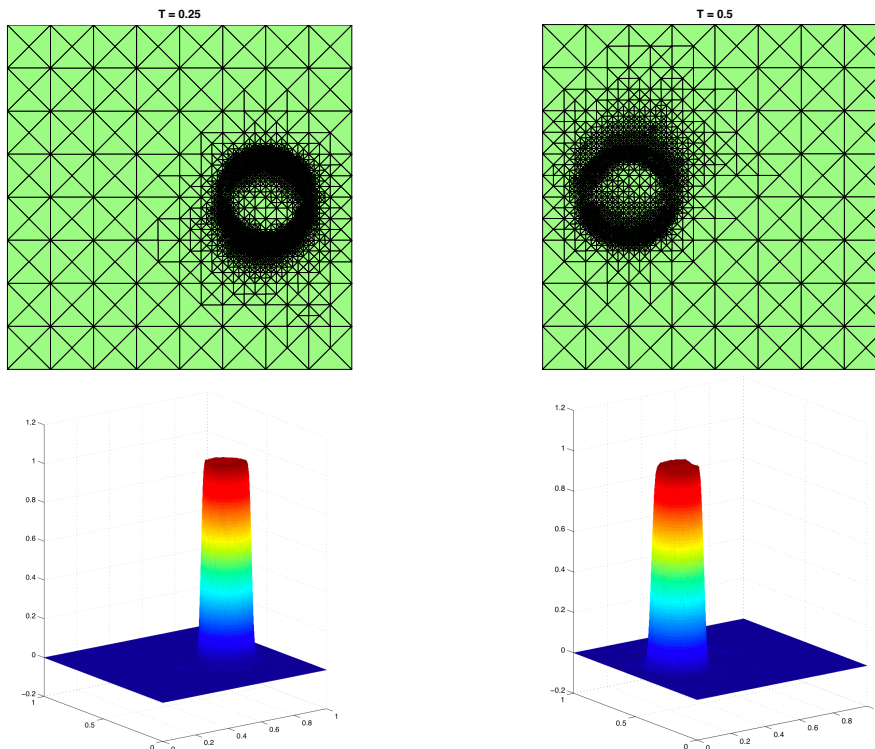


Fig. 6.8. Using Approach II with 33-point Gauss quadrature and the adaptive mesh refinement to solve Problem 6.5 ($\varepsilon = 10^{-4}$; left: $T = 0.25$, DOF = 3435; right: $T = 0.5$, DOF = 2330.)

approach and improves the accuracy. (4) And, less numerical diffusion is introduced by the finite element ELM, when more accurate integrations are used.

Acknowledgment. This work was done partly during the visit of the first and second authors to the Pennsylvania State University, University Park, supported by the China Scholarship Council. This work is supported in part by NSF DMS-0749202 and DMS-0915153. The authors would thank Prof. T. Russell and Prof. Y.-J. Lee for their valuable suggestions and comments.

References

- [1] J. Douglas, Jr. and T.F. Russell, Numerical methods for convection-dominated diffusion problems based on combining the method of characteristics with finite element or finite difference procedures, *SIAM J. Numer. Anal.*, **19**:5 (1982), 871–885.
- [2] O. Pironneau, On the transport-diffusion algorithm and its applications to the Navier-Stokes equations, *Numer. Math.*, **38**:3 (1982), 309–332.
- [3] T.F. Russell, Eulerian-Lagrangian Localized Adjoint Methods for advection-dominated problems, Numerical Analysis 1989: Proceedings of the 13th Dundee Conference, June 1989, pages 206–228, Longman Higher Education, 1990.
- [4] M. Celia, T. Russell, I. Herrera and R. Ewing, An Eulerian–Lagrangian localized adjoint method for the advection–diffusion equation, *Water Res.*, **13** (1990), 187–206.
- [5] A. Staniforth and J. Côté, Semi-lagrangian integration schemes for atmospheric models: A review, *Monthly Weather Review*, **119** (1991), 2206–2223.
- [6] T. Arbogast and M.F. Wheeler, A characteristics-mixed finite element method for advection-dominated transport problems, *SIAM J. Numer. Anal.*, **32**:2 (1995), 404–424.
- [7] P. Bartello and S.J. Thomas, The cost-effectiveness of semi-Lagrangian advection, *Mon. Weather. Rev.*, **124** (1996), 2883–2897.
- [8] T.F. Russell and M.A. Celia, An overview of research on Eulerian–Lagrangian localized adjoint methods (ELLAM), *Adv. Water Resour.*, **25** (2002), 1215–1231.
- [9] F. Russell, Numerical dispersion in Eulerian-Lagrangian methods, *Computational Methods in Water Resources*, **2** (2002).
- [10] E. Süli, Convergence and nonlinear stability of the Lagrange-Galerkin method for the Navier-Stokes equations, *Numer. Math.*, **53**:4 (1988), 459–483.
- [11] zhangchensong@gmail.com M. Bause and P. Knabner, Uniform error analysis for Lagrange-Galerkin approximations of convection-dominated problems, *SIAM J. Numer. Anal.*, **39**:6 (2002), 1954–1984.
- [12] K.W. Morton, A. Priestley and E. Süli, Stability of the Lagrange-Galerkin method with non-exact integration, *M2AN Math. Model. Numer. Anal.*, **22** (1988), 625–653.
- [13] E. Süli, Stability and convergence of the Lagrange-Galerkin method with non-exact integration, *The Proceedings of the Conference on the Mathematics of Finite Elements and Applications, MAFELAP VI*, (1988), 435–442.
- [14] S.P. Neuman, Adaptive Eulerian-Lagrangian finite element method for advection-dispersion, *Int. J. Numer. Meth. Eng.*, **20**:2 (1984), 321–337.
- [15] Z. Chen, R. Nочetto and A. Schmidt, A characteristic Galerkin method with adaptive error control for the continuous casting problems, *Comput. Method. Appl. M.*, **189**:1 (2000), 249–276.
- [16] P. Houston and E. Süli, Adaptive Lagrange-Galerkin methods for unsteady convection-diffusion problems, *Math. Comput.*, **70**:233 (2001), 77–106.
- [17] Z. Chen and G. Ji, Sharp L^1 a posteriori error analysis for nonlinear convection-diffusion problems, *Math. Comput.*, **75**:253 (2006), 43–71.
- [18] J. Xu, Iterative methods by space decomposition and subspace correction, *SIAM Rev.*, **34** (1992), 581–613.

- [19] A. Chorin and J. Marsden, A Mathematical Introduction to Fluid Mechanics, Springer-Verlag, 2000.
- [20] R. Warming and B. Hyett, The modified equation approach to the stability and accuracy analysis of finite-difference methods, *J. Comput. phys.*, **14** (1974), 159–179.
- [21] R.S. Varga, Matrix Iterative Analysis, Springer, 2000.
- [22] P.D. Lax and R.D. Richtmyer, Survey of the stability of linear finite difference equations, *Commun. Pur. Appl. Math.*, **9** (1956), 267–293.
- [23] L. Trefethen, Group velocity in finite difference schemes, *SIAM Rev.*, **24** (1982), 113–136.
- [24] R. Verfürth, A Review of a Posteriori Error Estimation and Adaptive Mesh Refinement Techniques, Wiley and Teubner, 1996.
- [25] A. Schmidt and K.G. Siebert, Design of Adaptive Finite Element Software, volume 42 of *Lecture Notes in Computational Science and Engineering*, Springer-Verlag, Berlin, 2005, The finite element toolbox ALBERTA.
- [26] L. Chen and C.-S. Zhang, AFEM@matlab: a Matlab package of adaptive finite element methods, Technical report, University of Maryland at College Park, 2006.
- [27] V. John and E. Schmeyer, Finite element methods for time-dependent convection-diffusion-reaction equations with small diffusion, *Comput. Method. Appl. M.*, **198** (2008), 475–494.
- [28] D. Xiu and G.E. Karniadakis, A semi-Lagrangian high-order method for Navier-Stokes equations, *J. Comput. Phys.*, **172**:2 (2001), 658–684.